



Minerva Access is the Institutional Repository of The University of Melbourne

Author/s:

Mondal, S;Disfani, MM

Title:

Lateral load-carrying mechanism of driven battered minipiles

Date:

2024-09-01

Citation:

Mondal, S. & Disfani, M. M. (2024). Lateral load-carrying mechanism of driven battered minipiles. *Acta Geotechnica*, 19 (9), pp.6407-6425. <https://doi.org/10.1007/s11440-024-02250-x>.

Persistent Link:

<https://hdl.handle.net/11343/352525>

License:

[cc-by](#)



Lateral load-carrying mechanism of driven battered minipiles

Sanchari Mondal¹ · Mahdi M. Disfani¹

Received: 21 February 2023 / Accepted: 11 January 2024 / Published online: 24 May 2024
© The Author(s) 2024

Abstract

The lateral load-carrying mechanism of vertically installed and battered minipiles is evaluated using 1g-physical and numerical modelling. Single minipiles with batter angles of 0° , $\pm 25^\circ$ and $\pm 45^\circ$ are tested under lateral load in medium dense and dense sand. The minipiles are instrumented with fibre Bragg grating optic fibres to obtain a strain profile (two-dimensional) along the minipile shaft. A calibrated numerical model is further adopted to produce p - y curves for battered minipiles at various node deflections. The ratio of soil reaction of battered minipiles to vertically installed minipiles is observed to change with both deflection and depth of the minipile. An analytical solution is developed based on the decomposition of lateral load into skin friction and passive pressure for battered minipiles. A reduction factor is proposed that considers a decrease in passive pressure when the minipile is loaded in the opposite direction of the batter. The analytical solution is capable of accounting for soil properties, pile rigidity and the angle of inclination of battered minipiles. The analytical method is subsequently verified for cohesive soils using full-scale field results. The ratio of the ultimate lateral load of battered minipiles to vertical minipiles presented in the literature corroborated the findings of this study.

Keywords Battered angle · Driven minipiles · FDM · Lateral load-carrying mechanism · Optic fibre

1 Introduction

Minipiles are hollow, shallow-depth piles that are driven into the soil, often in groups. They typically have a diameter of 42.4 mm and a length of up to two metres and are driven into the soil in battered (reticulated) configurations. Groups of three or more battered minipiles are used as foundations of light structures such as electric poles, solar panels and small wind turbines. They have recently become popular worldwide due to their lightweight and easy installation. To quantify the performance of these minipile groups, it is essential to understand the behaviour of single minipiles at shallow depths primarily.

Minipiles are characteristically similar to micropiles in physical attributes except without grouting. Micropiles are a small-diameter (normally less than 300 mm) deep

foundation system first introduced by Lizzi [38]. They have since been widely used to retrofit existing foundations and reinforce in situ earth structures due to their ease of installation in inaccessible areas [25]. In the micropile design and construction manual [7], the design of vertical micropiles subjected to lateral load is stated to be similar to that of a conventionally driven pile. The lateral load capacity of a pile can be analysed using various techniques like the p - y curve technique [39], strain wedge method [9] and the distribution of soil pressure in front of the piles. The mobilised passive pressure of rigid piles was investigated by Broms [15], Meyerhof and Yalcin [45], Fleming et al. [21], Prasad and Chari [51] for vertical piles and by Meyerhof and Ranjan [42], Meyerhof and Sastry [43] for battered piles under inclined loads. Meyerhof and Yalcin [45] reported the effects of inclined and eccentric lateral loading on flexible-type battered piles in the sand.

Battered piles/minipiles have higher lateral stiffness than vertical piles [24, 42]. The effect of batter angle on p - y curves was investigated by Kubo [29] and Awoshika [12] using full-scale and model tests in a tank, respectively. Based on their test results, they proposed a modifying constant as a function of the batter angle to increase or

✉ Mahdi M. Disfani
mmiri@unimelb.edu.au

¹ Department of Infrastructure Engineering, Faculty of Engineering and Information Technology, The University of Melbourne, Block B 207, Melbourne, VIC 3010, Australia

decrease the ultimate lateral resistance. However, the modifier did not account for the relative density (D_r) of the soil or rigidity of the pile, limiting its application in practice. Through centrifuge modelling, Zhang et al. [65] studied the effects of batter angle on flexible piles in dense and loose sand. They introduced a modifying factor for p – y curves, which was sensitive to the relative density of the soils. Kyung and Lee [32] also inspected the effects of the inclination of micropiles in the sand, and their investigation reported an optimum batter angle of 30° in dense sand to reach maximum load-carrying capacity. Sharma and Husain [58] experimentally studied the effect of the length (L) to diameter (D) ratio of grouted micropiles at various batter angles subjected to lateral load and reported an optimum L/D ratio of 48 for 30° batter angle, beyond which the increment in the micropile length had an insignificant effect. However, these above studies do not consider a wide range of either pile and soil properties or both, and hence, the proposed empirical factors might not be robust. A recent study by Ashour et al. [8] again suggested a multiplier from the strain wedge model for p – y curves of battered piles for sandy soils only, and its applicability for cohesive soil is not yet justified or investigated.

The overarching aim of this study is to investigate the effect of batter angle on the lateral loading capacity of micropiles in medium dense and dense sand. This is achieved by 1g-physical modelling through consideration of the stress-scale effect. The optical fibre instrumented micropiles were further used to calibrate numerical models to attain stress contours, axial force and bending moment distribution, which otherwise require heavy instrumentation during experimentation. The validated numerical model also produced p – y curves and p -multipliers at shallow depth for these scarcely studied shallow-depth micropiles. Finally, to translate the observations of this study to a more practical level, a modified classical analytical theory is proposed based on the experimental and numerical observations. The motivation is to elucidate the interaction of micropiles, especially when oriented in different directions respective to the loading at different batter angles in both cohesionless and cohesive soil. This study is aimed to address the research gap about shallow-depth battered micropiles under lateral loading in cohesionless soil and the lack of proper understanding based on limited reported data on battered piles.

2 1g Physical model

To investigate the soil–structure interaction of battered and vertical single micropiles under lateral loading conditions, small-scale model micropiles were tested in a sand tank in

controlled laboratory conditions. A test tank of 25-mm-thick cross-laminated plywood (braced internally with steel sections) was fabricated with a length and width of 1000 mm and a height of 600 mm, respectively (Fig. 1). Dry clean silica sand, classified as poorly graded sand (SP) according to the Unified Soil Classification System, was used in this study (Fig. 2). The maximum and minimum density, $\gamma_{d, \max}$ and $\gamma_{d, \min}$, were measured 18.3 kN/m^3 and 16.9 kN/m^3 [10, 11], respectively.

2.1 Methodology

The tank was filled with sand using the pluviation technique adopted from Rad and Tumay [52], as a high relative density of 92% was reported to be achieved using a similar sand pluviation technique earlier [30–32]. The components of the sand rainer, as shown in Fig. 3a, were first designed and fabricated. The setup had two main parts: a porous sand tray with a shutter to hold the sand before diffusing and two diffusers placed above the sand bed to deposit the sand evenly. The height between the shutter and the diffuser was designed to be adjustable. The distance between the shutter and the diffuser is called the falling distance, and the distance between the diffuser and the sand bed in the tank is called the falling height. The following factors affected the deposition intensity or the relative density of the sand in the tank: porosity of the shutter, diffuser type

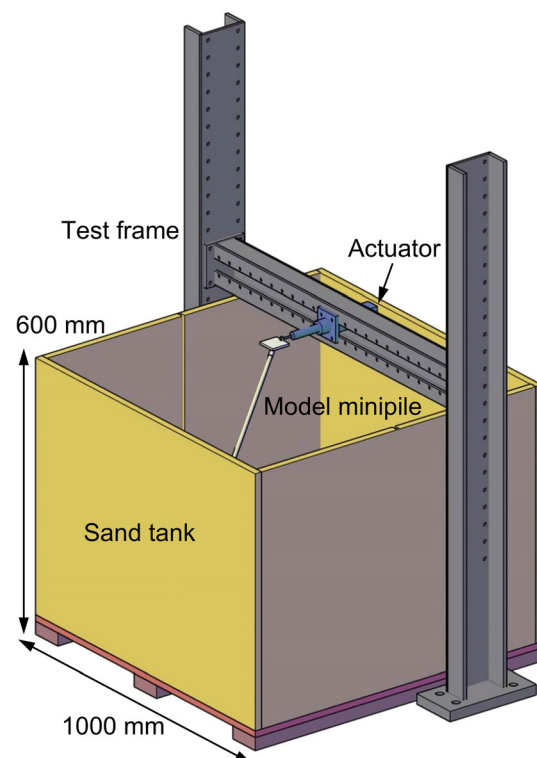


Fig. 1 Schematic of the test setup

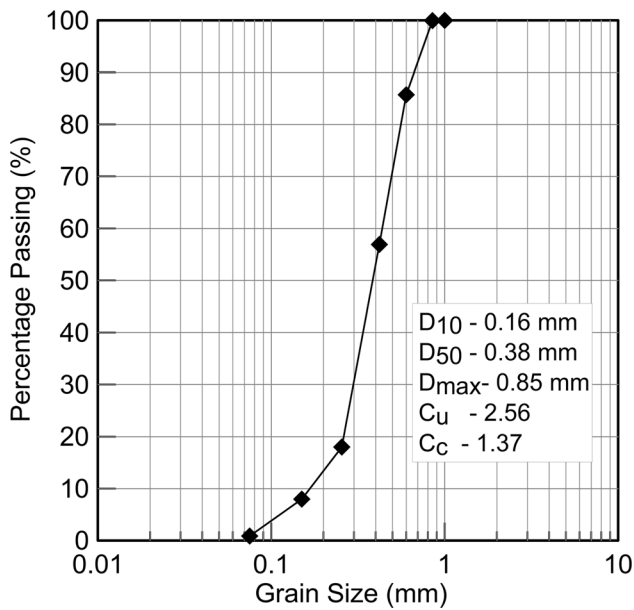


Fig. 2 Particle size distribution

and falling height. A shutter porosity of 1.54% and two sieves with an aperture size of 3.33 mm, placed 10 mm apart, were chosen based on a range proposed for maximum density [52]. Before filling the sand tank, a calibration process was completed to find the relationship between the relative density and fall heights (Fig. 3b). The falling height for 90% and 75% relative density was determined to be 400 mm and 200 mm, respectively. The falling distance was adopted from Rad and Tumay [52] and kept fixed at 500 mm because the sand reached its terminal velocity at

this distance. A constant falling height was adopted to fill sand in 50-mm-thick layers to achieve a uniform relative density. Thus, the diffuser sieves were lifted by 50 mm, and this was done twelve times to maintain the fall height while filling the 600-mm-deep tank.

2.2 Geometry of physical modelling and scale effects

2.2.1 Geometric scale

To understand the behaviour of a full-scale minipile with an outer diameter of 42.4 mm, a thickness of 2.5 mm and a length of 1.6 m in cohesionless soil, the model minipiles were geometrically scaled down. The outer diameter of the steel minipile was selected to be 9.54 mm, and the linear scale factor ($1/N$) of 4.44 was determined as the ratio of the diameter of the prototype to the model minipile. The length of the model minipile was estimated to be 360 mm following the Buckingham pi theorem [61]. As the area could not be practically factored down, the relative stiffness of the model minipile was maintained of the same order as that of a typical minipile. According to the equation proposed by Poulos [49], the relative stiffness of the pile (K_{rs}) can be determined by Eq. 1. This method has been widely applied earlier for calculating the relative stiffness of model piles with similar dimensions by Lee et al. [34] and Abadie et al. [2] among others.

$$K_{rs} = E_p I_p / E_{SL} L^4 \tag{1}$$

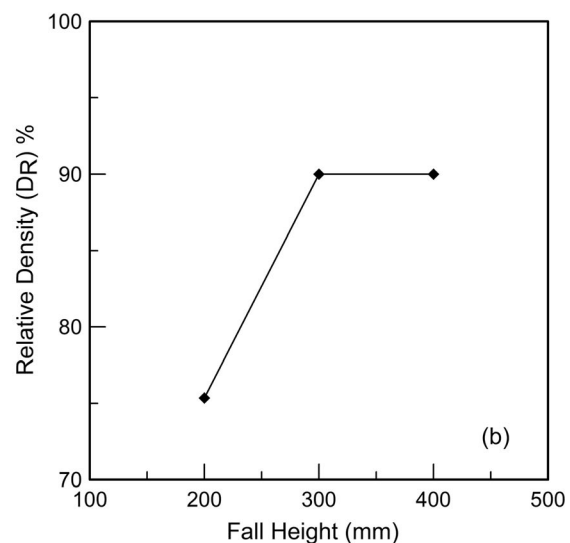
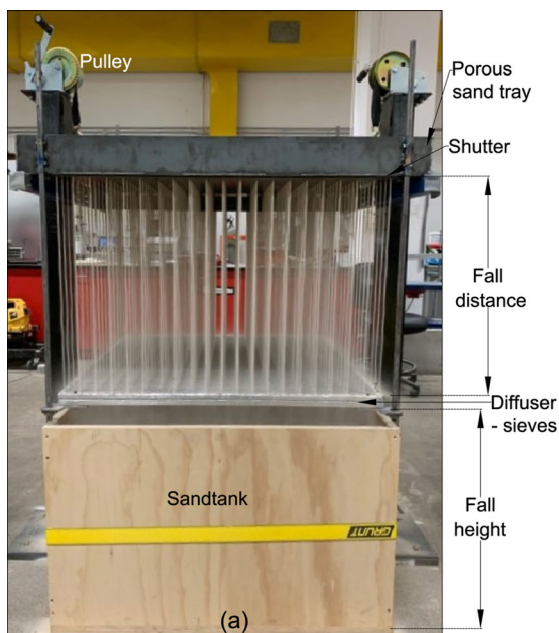


Fig. 3 a Pluviation setup and b calibration graph for various fall heights

where $E_p I_p$ is the flexural rigidity of the pile, E_{SL} is Young’s modulus of soil at the pile tip that can be calculated using $E_{SL} = 2(1 + \mu)G_0$, where G_0 is the small-strain shear modulus, and L is the embedded depth of the pile [2]. The G_0 was obtained experimentally in this study, and E_{SL} was then determined from the given relation. E_{SL} corresponding to 90% relative density at the desired effective vertical stress was established from the experimental data, as described in the following section. When the relative stiffness of the pile is between 0.208 and 0.0025, the pile can be considered semi-rigid [2]. The K_{rs} of the driven minipiles studied here, according to Eq. 1, is 0.00395, so it can be classified as a semi-rigid minipile.

2.2.2 Stress scale

In 1g model tests, due to low confining pressure compared to field conditions, the soil density is reduced to represent the soil dilatancy in the field for conventional piles [2, 6, 33]. However, for studies on model micropiles [30], scaling of stress has not been reported earlier, most likely due to the shallow depth of the prototype micropiles themselves. In this study, the peak friction angle, dilation angle and Young’s modulus of soil were estimated from direct simple shear tests (DSS) as deformation along the pile shaft resembles the simple shear condition [4].

NGI-type simple shear device [14] was used to perform the simple shear tests over a range of normal stresses from 25 to 150 kPa at three different relative densities (75, 90 and 100%), as shown in Fig. 4a, 4b. The internal friction angle was calculated per $\tan^{-1}(\tau_{xx}/\sigma'_z)$ based on the assumptions mentioned and justified in Al Tarhouni and Hawlader [5]. The friction angle versus effective vertical stress was logarithmically fitted, and the soil’s Young’s

modulus was fitted using a power law with an exponent equivalent to nearly one. The relationship between Young’s modulus and the effective vertical stress seems almost linear, as stiffness parameters were measured only over a narrow range of vertical stresses. This piecewise linear relationship between shear modulus and normal stress over a narrow range of normal stresses is also illustrated in Wang and Mok [62].

The shear parameters at even lower stress levels were extrapolated, as was also reported by Leblanc et al. [33]. The effective vertical stress at 100% D_r for the prototype minipile of 1.6 m length is 29.3 kPa, and considering the same unit weight of the soil, the maximum representative effective stress for the model minipile of 0.36 m length is 6.6 kPa. From Fig. 4a, the peak friction angle at around 6.6 kPa normal stress for 90% D_r (1g condition) is 39°, and the relative density corresponding to 39° peak friction angle at around 30 kPa is 100%, representing very dense field condition. Similarly, from Fig. 4b, the estimated Young’s modulus of soil at 1g level is 0.95 MPa. Along with the peak friction angle (ϕ), the critical state friction angle (ϕ_c) was obtained from the experimental data, and consecutively, the dilation angle (ψ) was estimated equal to $(\phi - \phi_c)/0.6$ as proposed by Chakraborty and Salgado [17] at low confining pressure.

Thus, considering a very dense field condition for the prototype minipiles, two dense but realistic relative densities of 90% and 75% were adopted in this study. Also, since the effect of batter angle is only significant in medium dense and dense sand [65], the relative density for the model could not be reduced any further. Nevertheless, the main cornerstone of this study is to compare the effect of batter angles at similar soil conditions. The force–displacement curves are presented henceforth adopting the

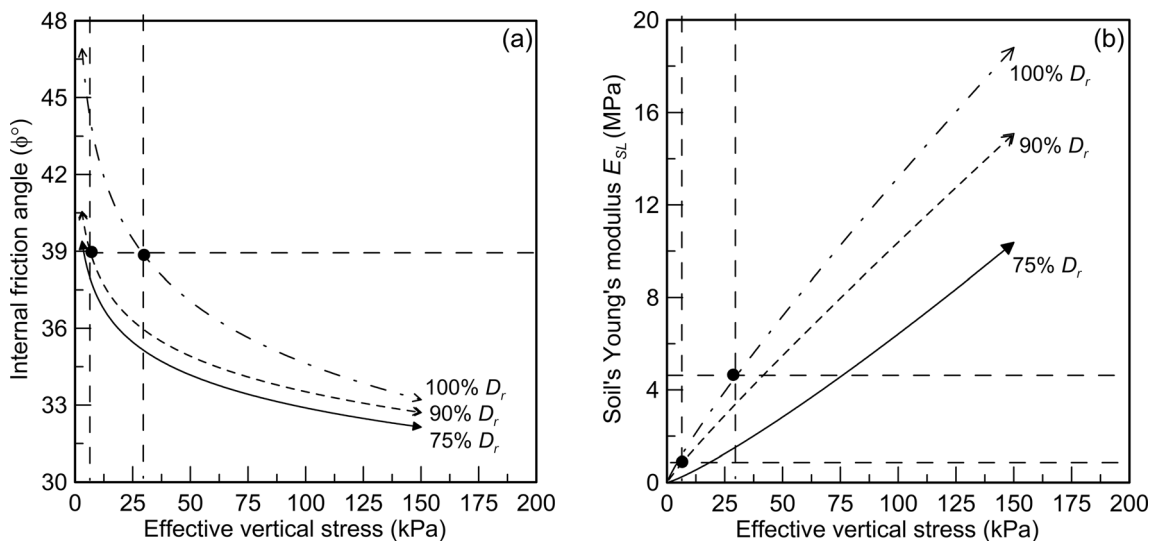


Fig. 4 a Internal friction angle and Young’s modulus as a function of relative density and effective vertical stress

dimensionless framework [33] to compare stress across various scales and soil properties as shown in Eq. 2 and Eq. 3,

$$\text{normalised force, } \bar{H} = \frac{H}{L^2 B \gamma'} \quad (2)$$

$$\text{normalised displacement, } \bar{u} = \frac{u}{B} \quad (3)$$

where H , γ' , L and B are the horizontal force, unit weight of the soil, length and diameter of the minipile, respectively.

2.2.3 Boundary effect

The minimum distance between the pile and the walls of the tank was maintained greater than $10B$ for minimum boundary effects, as also suggested by Poulos and Davis [50], Rao et al. [54] and Baek et al. [13], among others. The pile diameter (B) to the representative particle size of the sand (D_{50}) ratio should be greater than 20 for the particle size effect to be insignificant [64] and in this study, it was 25.

2.3 Instrumentation with optic fibre

Fibre Bragg grating optic fibre technique was employed for obtaining strain along the minipile shaft owing to its high spatial resolution compared to the conventional strain gauges. Traditional instrumentations such as strain gauges have drawbacks like large gauge sizes due to the length of the strain gauges. Thus, this study used robust optic fibre sensors due to their superior sensing technique [19]. Fibre Bragg grating (FBG) optic fibres have found their use in temperature and strain monitoring because of several advantages over traditional instrumentation techniques. They are lightweight, easy to install and have the feature of having several measurement points over small physical dimensions. These advantages reduce the excessive use of cables given the already smaller diameter of minipiles. The working principle of the FBGs is based on Bragg's law laid by W.H. Bragg and W.L. Bragg [36]. The FBGs in an optic fibre have a periodic modulation of refractive index, and when broadband light is incident on the optic fibre, the central wavelength matching that local modulation period is reflected [28]. The reflected central wavelength shifts when the optic fibre is subjected to strain and temperature change. The relation between the central Bragg wavelength and the strain under constant temperature [48] is shown in Eq. 4.

$$\frac{\Delta \lambda_B}{\lambda_B} = (1 - p_{\text{eff}}) \Delta \varepsilon \quad (4)$$

where $\Delta \lambda_B$ denotes the shift in central Bragg wavelength, p_{eff} is the photo-elastic parameter and $\Delta \varepsilon$ is the strain. Thus, the strain or temperature change can be obtained from the shift in wavelength.

Fibre optic sensors have been used earlier by other researchers to monitor full-scale pile or minipile behaviour (Mondal et al., 2022). Lee et al. [35] studied the feasibility of optic fibre instrumentation on piles in laboratory and field conditions and reported local axial strain as a function of wavelength shift. Li et al. [36] monitored and analysed pipe piles under hydraulic jacking using FBG sensing technology and reported the strain distribution along the pile. A similar approach has been adopted to instrument model minipiles with FBG-based optic fibres in this study.

Two arrangements of the FBGs were adopted for the tests; one pipe was instrumented with seven FBG, which was used for dense soil conditions (Fig. 5). When the tests were repeated at 75% relative density, all the minipiles were instrumented with six FBGs only starting at 110 mm below minipile head, as the contribution of the FBG above the soil surface was redundant. The optic fibres were attached to the surface of the minipile with adhesive owing to their very small diameter of 0.25 mm.

A calibration process was undertaken with two types of adhesives based on the literature: (a) cyanoacrylate and (b) two-part epoxy [60] to opt for an adhesive with a minimum strain loss. This study performed a three-point bending test on a model minipile on which one optic fibre with two FBGs was glued using cyanoacrylate. Two strain gauges with 2 mm gauge length were also installed adjacently to find the correlation between the wavelength shift and measured strain, as shown in Fig. 6. The same procedure was followed for two-part epoxy. The face on which the FBG and strain gauges were installed was subjected to both tension and compression, respectively. The plot (Fig. 7) shows the correlation between strain and wavelength shift, suggesting from the high coefficient of determination (R-squared) that either of the adhesives could be chosen. The cyanoacrylate adhesive was used in this study as the intercept was smaller. The relationship between the shift of wavelength and strain obtained from the calibration is shown in Eq. 5,

$$\mu \varepsilon = 281.97(\Delta \lambda) - 0.8932 \quad (5)$$

where $\mu \varepsilon$ is the microstrain and $\Delta \lambda$ is the shift in wavelength from the corresponding FBG. Even though the data points on the tension face corresponding to the negative wavelength shift are limited, the proposed relation can still produce reliable data. It is because only the compression face of the minipiles was instrumented for the lateral load tests in this study, as demonstrated in the following section. The shift in wavelength due to temperature change was neglected as the testing procedure was completed

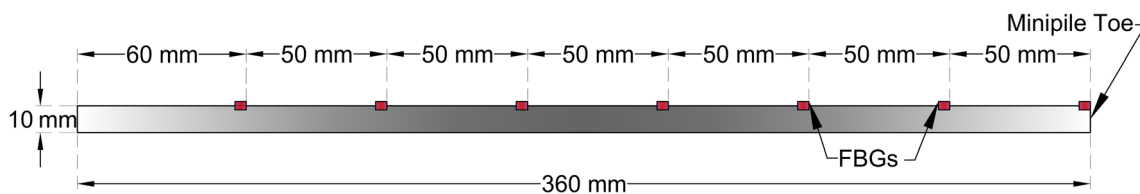


Fig. 5 FBG arrangement for the minipiles

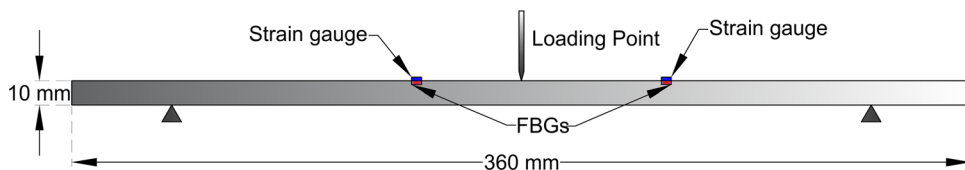


Fig. 6 Location of FBG and strain gauge for calibration

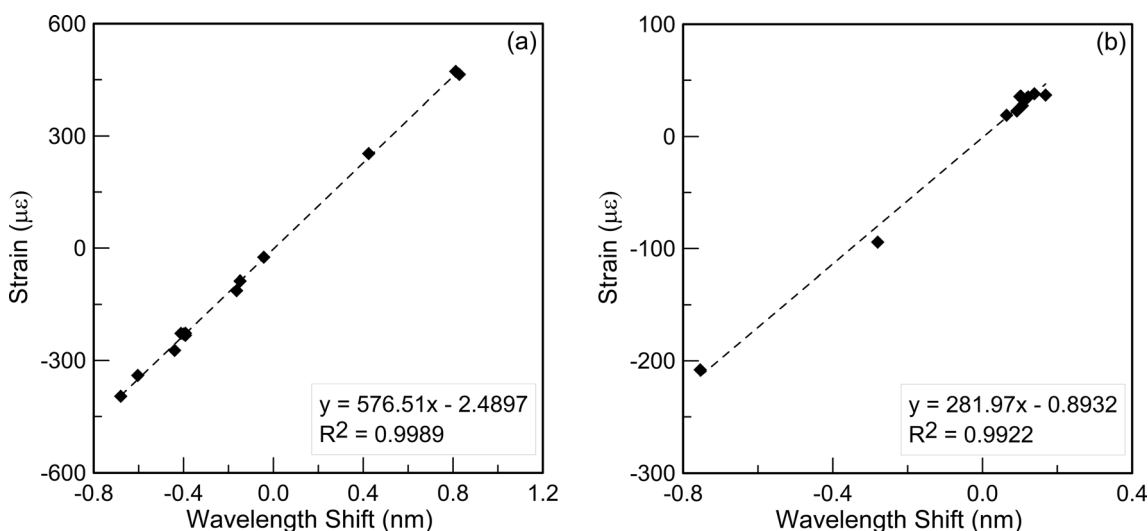


Fig. 7 Correlation between strain and wavelength shift for a epoxy and b cyanoacrylate adhesives

within a short period and in the laboratory’s controlled environment.

2.4 Test procedure

The single minipiles with three battered angles ($\theta = 0^\circ, 25^\circ$ and 45°) with respect to the vertical were tested under lateral loading at two different relative densities of 90 and 75%, as shown in Fig. 8. The minipile battered in the direction of load, i.e. $+25^\circ, +45^\circ$, and in the opposite direction, $-25^\circ - 45^\circ$, subsequently, will be addressed as positive and negative battered cases, respectively (Fig. 8a and c). The minipiles were installed with gentle, repeated blows using a rubber mallet hammer to replicate the field installation technique of full-scale steel minipiles using a jackhammer. A hole of 11 mm diameter battered at the three mentioned angles was drilled through thick plywood and used as a guiding frame to drive the minipiles at the

desired angle. The minipiles were driven into the soil up to a depth of 270 mm with a free head (eccentricity) of 90 mm. The effects of other types of installation were not considered in this study.

The minipile cap was attached rigidly to an actuator with a load cell of 10 N least count, and a digital indicator was connected to the cap to record lateral displacement. Laser sensors were also used to measure and validate the displacement of the pile cap. The load was applied at an increment of 0.01 kN (least count of the load cell) and maintained for 15 minutes with the aid of an actuator until the lateral displacement stabilised. An automatic closed-loop system with control and data logging software was used to operate the actuator to apply and record the load. The strain at discrete points along the minipile shaft was recorded at each loading stage from the optic fibre using an interrogator. As the interrogator had only one working channel, only one face of the minipile was instrumented

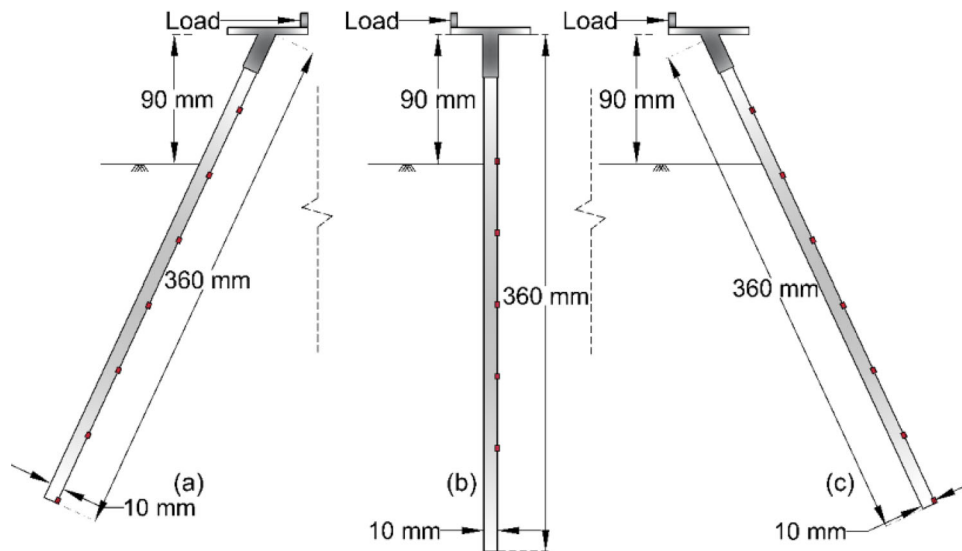


Fig. 8 Loading direction for **a** positive, **b** vertical and **c** negative battered minipiles

and recorded. This limitation was further overcome with the help of calibrated numerical models, as described in the *Numerical model* section.

2.5 Results and discussion

2.5.1 Load displacement curve

The normalised load–displacement curve of the positive, negative battered and vertically installed minipiles subjected to lateral load at 90% and 75% D_r are shown in Fig. 9a and b, respectively. The model minipiles were loaded until a maximum head displacement of 10–14 mm to avoid permanent deformation or bending of the

minipiles. Each test was repeated twice to confirm its repeatability, and only one of them (for brevity) depicting the repeated test results for vertical minipiles is shown in the plot (Fig. 9a).

The ultimate load capacity of laterally loaded micropiles is specified at various corresponding displacements. Abd Elaziz and El Naggar [3] proposed displacements of 6.25 mm, 12 mm or 5% of the diameter of the micropile for model micropiles; however, a displacement of 60% of the pile diameter was specified by Fukui [23]. Kyung and Lee [32] established the ultimate load at 3 mm displacement for their model micropiles of 5 mm diameter. In this study, the lateral ultimate capacity was chosen at 20% of the minipile diameter equal to 2 mm, according to Broms [15], as a

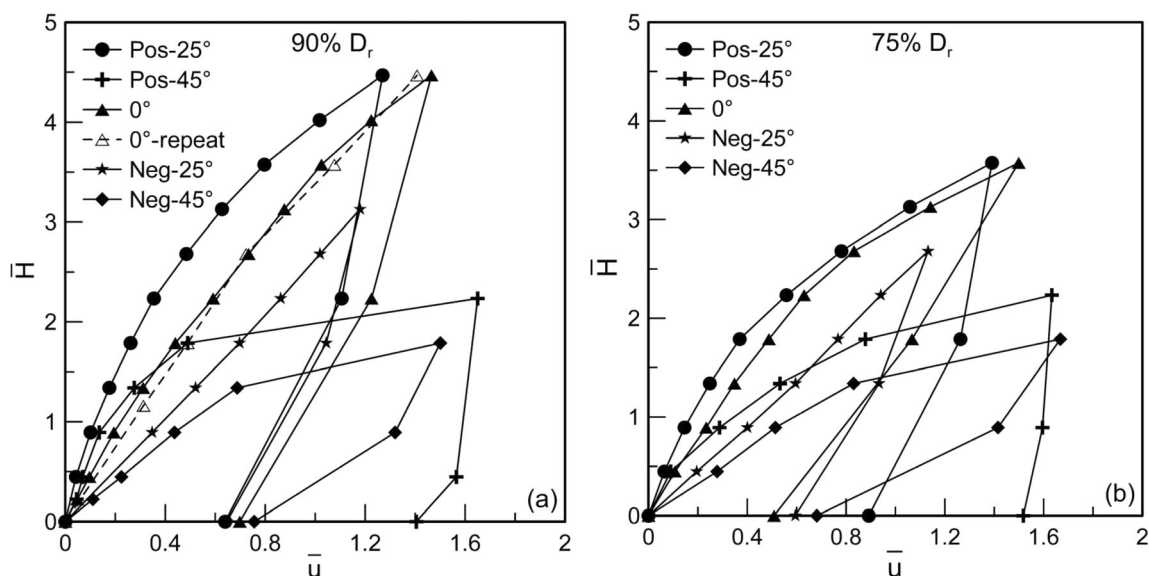


Fig. 9 Normalised load–displacement curve at **a** $D_r = 90\%$ **b** $D_r = 75\%$

displacement of $0.2B$ was believed to be a more relevant failure criterion for these small-diameter minipiles. Accordingly, the lateral capacity of the 0° , $+25^\circ$, $+45^\circ$, -25° and -45° minipile was found to be 20 N, 34 N, 25.2 N, 12 N and 10 N, respectively, for D_r of 90%. The $+25^\circ$ has maximum lateral resistance followed by $+45^\circ$, while the negatively battered minipiles have lower lateral resistance, with -45° being the least. The trend seems to change at higher displacement ($\bar{u} > 0.42$) as the force–displacement curve of $+45^\circ$ minipile reaches the plastic state.

For 75% D_r , the lateral resistance at 2 mm lateral head displacement for 0° , $+25^\circ$, $+45^\circ$, -25° and -45° was 18 N, 26 N, 16 N, 11 N and 8 N, respectively, as depicted in Fig. 9b. For 45° battered minipiles, not only the ultimate lateral load is lowest, but at each loading stage, the lateral displacement was also significantly higher compared to other battered minipiles. The general trend in the load–displacement curve depicts that, as the relative density of the sand was reduced, there was an anticipated decrease in the lateral resistance of the minipiles. The divergence among the load–displacement curves of various batter angles reduced with the lowering of the relative density of the soil as well. The lateral load capacity for 0° , $+25^\circ$, $+45^\circ$, -25° and -45° battered minipiles decreased by 10, 24, 37, 8 and 20%, respectively, when the density of the sand was reduced from 90 to 75%. This can be attributed to the fact that due to looser compaction, the sand in front of the minipile undergoes volumetric compression, and the soil pressure wedge is less mobilised than denser sand. There is also a clear contribution of the skin friction due to which the reduction percentages for all batter angles differ, which is further discussed in the *Analytical solution* section.

2.5.2 Strain profile

To compare the soil–structure interaction, the observed compressive strain profile along the minipile shaft at different loading stages is plotted in Fig. 10 at D_r of 90 and 75% for $\pm 25^\circ$. Figure 10a and b compares the strain profile at the equivalent loading stage at 90% D_r for $+25^\circ$ and -25° minipile, respectively. Similar plots are also presented for $+25^\circ$ and -25° battered minipile in Fig. 10c and d for 75% D_r . As evident from the strain profiles, the induced strain increases at each loading stage and the maximum value is observed at a depth of around 200 mm below the minipile tip. At equivalent force, the strain sustained by -25° minipile is highest, followed by 0° and $+25^\circ$, respectively. For instance, at 90% D_r , corresponding to 0.07 kN load, the strain recorded for -25° is $334 \mu\epsilon$, 0° is $297 \mu\epsilon$, and $+25^\circ$ is $224 \mu\epsilon$. This behaviour can be attributed to higher displacement for -25° and 0°

compared to $+25^\circ$ at the same applied lateral force, as shown in Fig. 9a. The trend observed for the minipiles in loosely compacted soil at 75% relative density is similar to that of 90% D_r . However, the magnitude of the strain recorded is comparatively lower than that for the dense sand condition because of the lesser lateral load resistance at lower relative density. The reduced strain is caused due to the reduction in lateral soil pressure and skin friction at 75% D_r , as described in the *Analytical solution* section.

The minipile–soil interaction at a particular displacement can be considered to compare the strain for battered cases. Since the ultimate load was measured corresponding to 2 mm lateral head displacement, the equivalent strains are plotted in Fig. 11 for further comparative analysis. The optic fibre results depict that the strain is higher for the positive condition followed by vertical and negative conditions at any particular displacement for both soil densities. When the relative density was reduced from 90% D_r to 75% D_r , the respective reduction in strain for 0° , $+25^\circ$ and -25° battered minipiles at 2 mm lateral head displacement reflected the load–displacement pattern presented earlier. The higher strain induced in the $+25^\circ$ minipile indicates higher mobilised passive pressure in front of the minipile at the same lateral displacement. The depth of maximum strain for 0° and -25° is deeper than that for $+25^\circ$ due to the lower relative stiffness of the latter at the same lateral displacement. Figure 11 also presents the strain profile for minipiles battered at $+45^\circ$ and -45° , where it is noted that the point of maximum strain shifts towards the minipile toe, supposedly due to the transition of minipile's relative stiffness from semi-rigid to rigid. The strain experienced for 45° is much lower than 0° , $+25^\circ$ and -25° , and this is due to lower mobilised passive pressure in front of the minipile at 45° which is later observed from p – y curves as well. As only one face of the minipile was instrumented, the bending moment could not be directly estimated, and the numerical model (described next) was used to compensate for this limitation.

3 Numerical model

A three-dimensional, explicit, finite difference program, FLAC^{3D} [1], was used to simulate the behaviour of model minipiles in dense (90% D_r) cohesionless soil. The overarching aim of the numerical model was to extract parameters such as stress contours, bending moment, axial force and p – y curves, which could not be directly obtained from the instrumentation. The numerical model was calibrated against the experimentally obtained force–displacement curve and strain profile for each batter angle, which was further adopted to extract additional quantities for deciphering the soil behaviour.

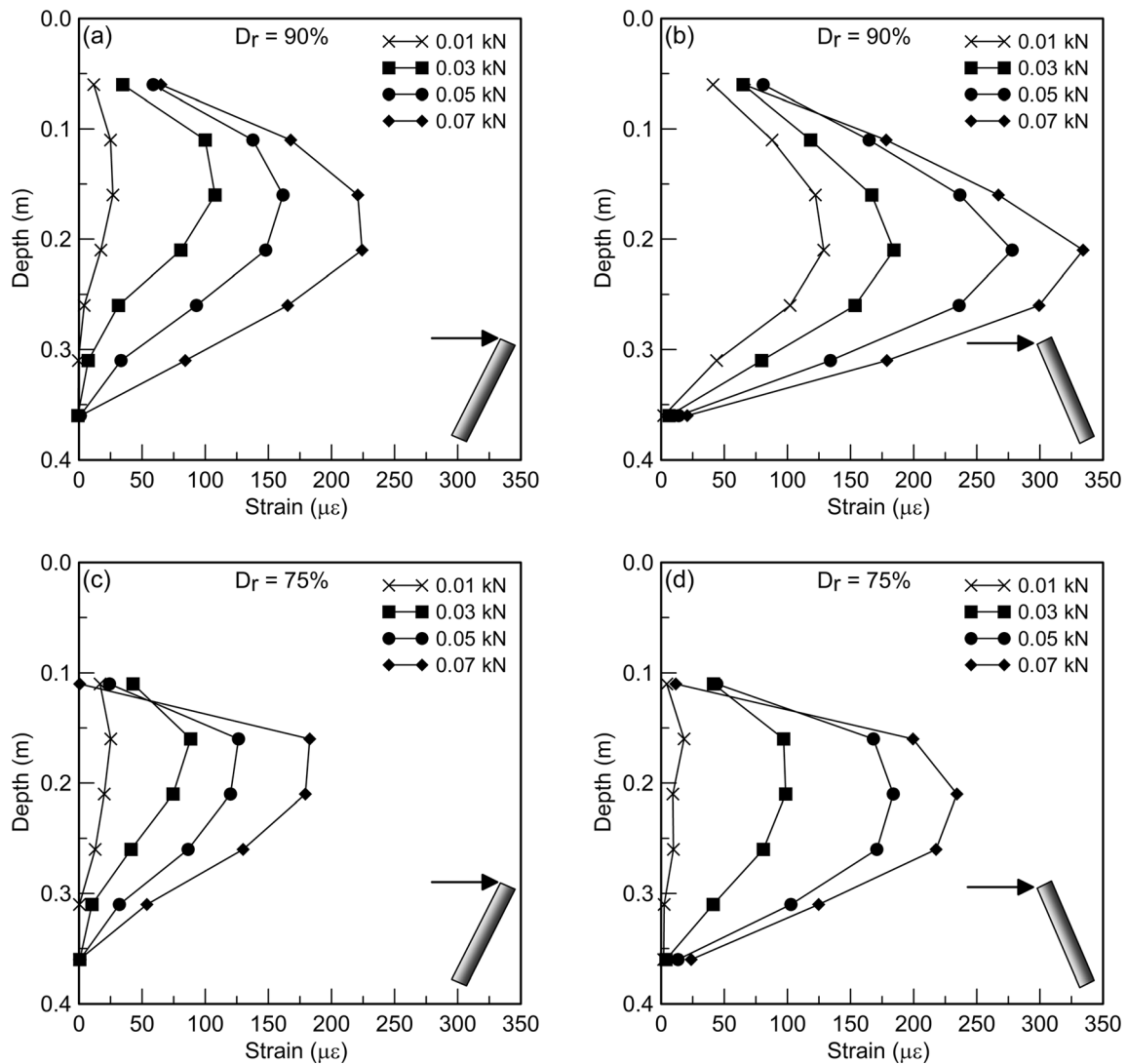


Fig. 10 Strain profile (compressive) along minipile shaft at 90% D_r (a, b) and 75% D_r (c, d) for $+25^\circ$ and -25°

3.1 Methodology

The minipiles were modelled using the pile structural elements, straight segments with uniform and bi-symmetrical cross-sectional properties between two nodes. A hexahedral brick-shaped mesh type with eight vertices was used to model the soil. The mesh size was optimised after performing sensitivity analysis, in which the mesh size was changed from coarse to finer; the optimum mesh size beyond which the change in lateral displacement (for two consecutive analyses) was less than 3% was chosen [27]. The square soil zone had a length of 100 times the minipile diameter (B), and the distance from the minipile toe to the base of the soil was more than $20B$, which is significantly greater than the values proposed in the literature [13, 20, 27, 50]. The soil was modelled with roller boundaries at the sidewalls and fixed and free boundaries at

the base and top face, respectively. The initial stresses in the soil zone were initialised with a coefficient of earth pressure of 0.37, calculated using the relation $K_0 = 1 - \sin\phi$ [40].

An elastoplastic Mohr–Coulomb constitutive model was used to simulate the soil, as it can accurately predict ultimate failure criteria with only basic soil parameters. The properties of the minipile used for the numerical model are presented in Table 1, and the soil properties estimated from laboratory tests (as elaborated earlier) are summarised in Table 2.

The interaction between the pile and soil was modelled using coupling springs, which act in the normal and shear direction at the interface. The coupling gap in the normal direction was set ‘on’ to allow pile–soil separation. The end-bearing mechanism can be modelled by defining a spring between the structure and the grid at the pile toe.

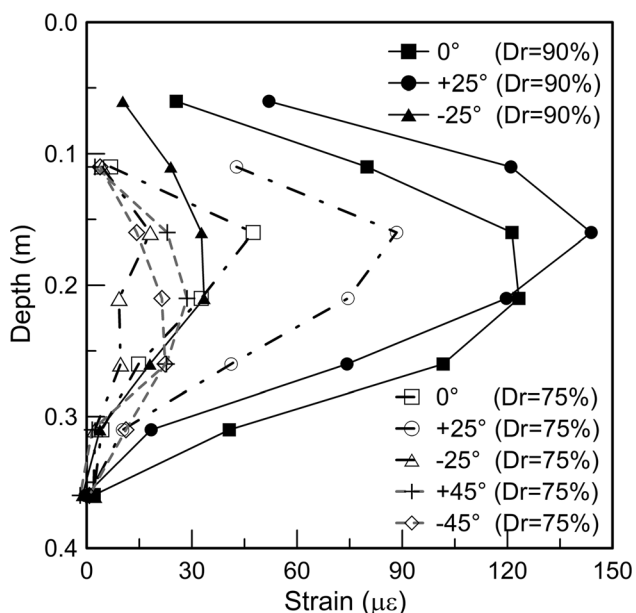


Fig. 11 Strain profile at 2 mm lateral displacement for all batter angles

The springs have both cohesive and frictional properties, and their controlling parameters are stiffness (k_s and k_n), cohesion per unit length (c_s and c_n) and friction (φ_s and φ_n) in both shear and normal direction, respectively, to the pile–soil interface. The stiffness parameters out of these six values require calibration for changes in loading directions [1].

The numerical model developed was validated with the respective force–displacement curves and strain profiles obtained from physical modelling by calibrating the spring parameters. The cohesive strength per unit length (c_s and c_n) was assigned a value of 1 kPa, and φ_s and φ_n were assumed to be 0.8ϕ [18] or 31.2° as the interface friction angle between the steel and dense sand for all batter angles. The model was calibrated for each batter angle, assuming an initial value for the stiffness parameters, k_s and k_n , based on the relations mentioned in Mondal et al. [46], as proposed by Randolph [53]. Then, several iterations were performed using a trial-and-error method until the computed and experimentally observed load–displacement curve and strain profile coincided. The value of k_s and k_n

Table 2 Properties of the cohesionless soil

E_{sL}^a (N/m ²)	γ^b (kN/m ³)	φ^c (°)	ψ^d (°)	c^e (N/m ²)	μ^f
0.94×10^6	18.1	39	4.9	0	0.30

^aYoung’s modulus ^cinternal friction angle ^ecohesive strength

^bUnit weight of soil ^ddilation angle ^fPoisson’s ratio

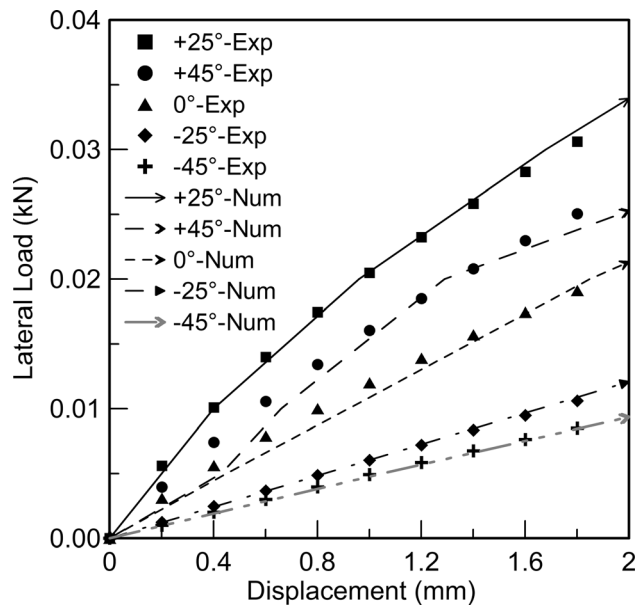


Fig. 12 Comparison of numerically obtained force–displacement curves with lg tests

were 1×10^9 , 2.4×10^5 , 5×10^8 , 1.2×10^5 and 4×10^4 , respectively, for +25°, +45°, 0°, –25° and –45° batter angles. After calibration, the decreasing order of k_s and k_n of the battered minipiles (excluding 0°) was found to be consistent with the order of their respective experimental ultimate lateral load capacities. The load–displacement curves suggested a very good agreement between the experimental and numerical results owing to the appropriate choice of stiffness parameters at the interface (Fig. 12). The validated numerical model was then used to predict the p – y curves of the battered minipiles.

Table 1 Mechanical properties of the minipile used in FLAC^{3D}

E_p (N/m ²)	Area (m ²)	Perimeter (m)	I_y^a/I_z^b (m ⁴)	J^c (m ⁴)	μ^d
2×10^{11}	7.07×10^{-6}	0.03	3.12×10^{-10}	6.24×10^{-10}	0.33

^aSecond moment with respect to y-axis ^cpolar moment of inertia

^bSecond moment with respect to z-axis ^dPoisson’s ratio

3.2 Results and discussion

3.2.1 Shallow-depth p - y curves for battered minipiles

The minipiles' batter angle significantly affects their lateral load behaviour at shallow depths [8], which can be well determined using p - y curves. The bending moment profiles for all the battered angles were extracted from their respective calibrated numerical models. Figure 13a shows that the bending moment increases up to a depth of 0.18 m below the pile tip, and the maximum bending decreases in magnitude in the following order of batter angles, $0^\circ > +25^\circ > -25^\circ > +45^\circ > -45^\circ$. As the vertical minipile does not carry any axial load, the total strain sustained is the bending strain only. However, for battered minipiles, a fraction of the lateral load is converted to the axial component, contributing to axial strain. Therefore, at 2 mm displacement, the total strain measured from optic fibre for $+25^\circ$ was higher than 0° (Fig. 11); however, the bending moment for vertical minipile at the same 2 mm displacement is 28% higher due to no strain decomposition.

The mobilised passive pressure per unit length, p , in front of the minipile is extracted from the bending moment (Fig. 12b) using the relation [63],

$$p(z, t) = -\frac{d^2M(z, t)}{dz^2} \quad (6)$$

where z and t are the pile depth and time, respectively, and the lateral deflection, $y(z, t)$ is obtained directly from the numerical model at each node. The maximum p at 2 mm lateral head displacement decreases in the following order of batter angles: $+25^\circ > 0^\circ > -25^\circ > +45^\circ > -45^\circ$. The resisting pressure distribution on the passive side of the minipiles is almost triangular, as proposed by Lin et al.

[37] and Sastry and Meyerhof [57] for laterally loaded piles in sand. The larger the mobilised passive pressure wedge area, the higher the ultimate lateral resistance.

The p - y curves at $5B$ and $10B$ depth, up to a lateral deflection of 2 mm (at the respective nodes), are presented in Fig. 14a and b, respectively, for all the battered angles. The ratio of soil reaction of battered minipile, p_B , to that of vertical minipile, p_v , represented as Ω [8, 29, 65] was also evaluated at lateral node deflection of 0.5, 1, 1.5 and 2 mm, and is summarised in Table 3. In contradiction to what has been reported in the literature, Ω is less than one for positive and negative battered, shallow-depth, semi-rigid minipiles at a depth of $5B$ from the soil surface. However, at a depth of $10B$, Ω is higher than one for $+25^\circ$, increasing further with lateral displacement. The $+45^\circ$ battered minipile does not offer a higher soil reaction compared to the vertically installed minipile. However, this behaviour was only observed for dense sand, and other relative densities require further investigation.

3.2.2 Axial force and horizontal stress contour

The mobilised passive pressure in front of the minipile is extracted from the numerical model and shown in Fig. 15. The maximum σ_{xx} decreases in the following order of batter angles, $+25^\circ > 0^\circ > +45^\circ > -25^\circ > -45^\circ$. The decreasing order of magnitude and nature of the soil pressure distribution at 2 mm lateral head displacement is in agreement with the strain profile comparison for dense sand, as shown in Fig. 11. From the numerical model, the structural displacement vectors (Fig. 15) indicated that for positive battered minipiles, the displacement vector points upwards along the inclination axis as the depth increases. Contrarily, in the negative case, the pile tends to move into

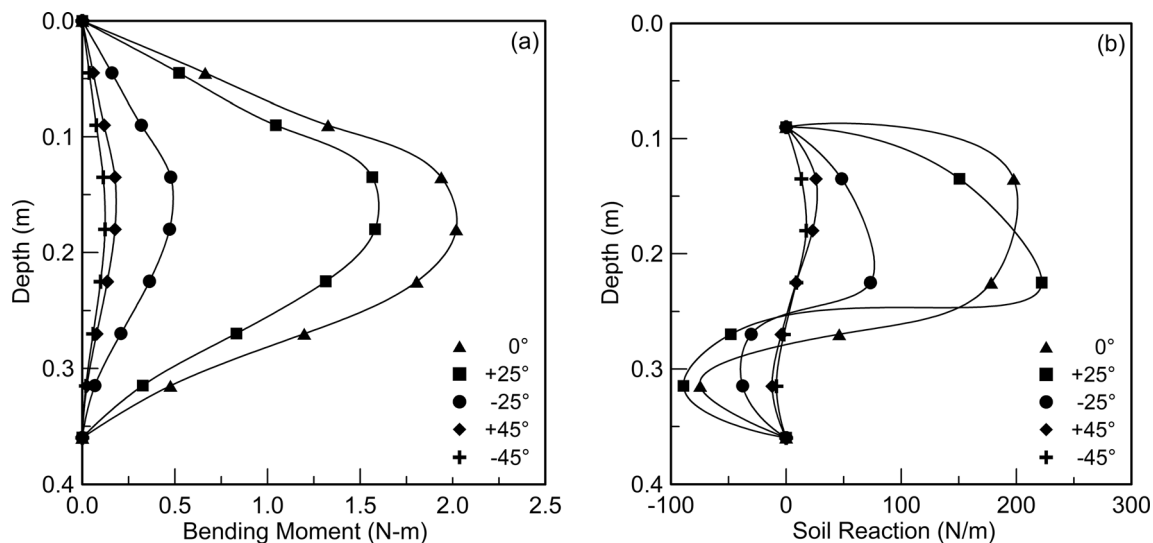


Fig. 13 Bending moment and soil reaction profile at 2 mm lateral head displacement

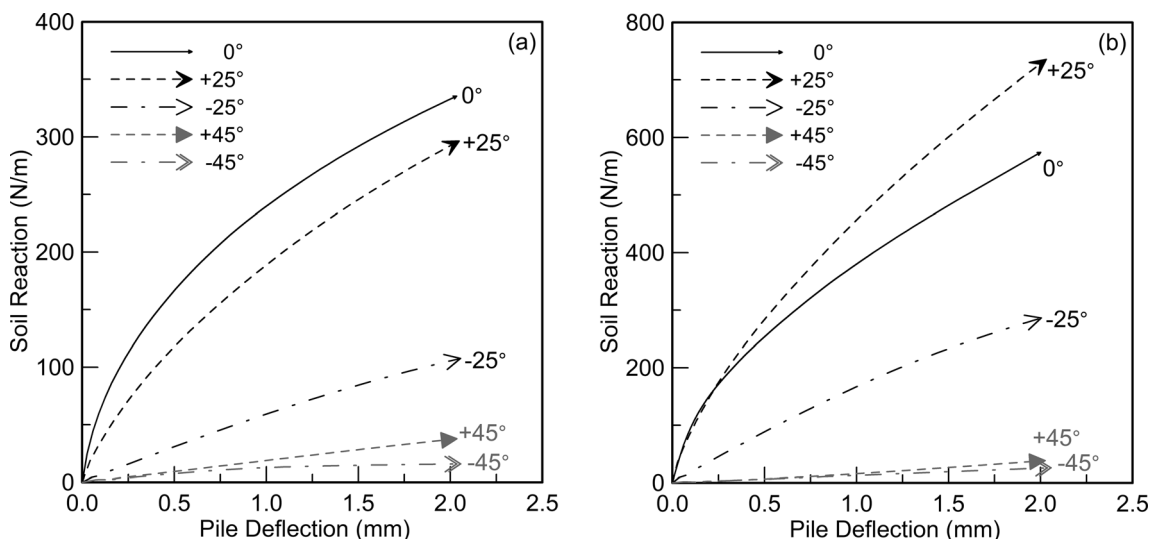


Fig. 14 *p*-*y* curves at a 5B and b 10B depth from the soil surface

Table 3 Ratio of ultimate soil reaction (Ω)

Angle	Depth—5B				Depth—10B			
	Deflection (mm)							
	0.5	1.0	1.5	2	0.5	1.0	1.5	2
0°	1.00	1.00	1.00	1.00	1.00	1.00	1.00	1.00
+ 25°	0.71	0.79	0.84	0.88	1.12	1.20	1.25	1.32
- 25°	0.19	0.25	0.29	0.32	0.35	0.44	0.48	0.52
+ 45°	0.06	0.08	0.10	0.11	0.03	0.04	0.05	0.07
- 45°	0.05	0.05	0.05	0.05	0.03	0.03	0.04	0.05

the soil along the axis of the batter when subjected to lateral load. This observation will be used to describe the direction of the decomposed loads used further in the Analytical section.

The battered minipiles have higher lateral resistance than vertically installed minipiles due to the conversion of lateral load into an axial component resisted by the skin friction along the minipile shaft. From the axial load distribution obtained using the numerical model, the mobilised skin friction for positively battered minipiles is higher than that of negatively battered minipiles at ultimate capacity. The maximum axial load is carried by + 25°, and the vertical minipile sustains almost zero axial load. The axial load maintained by + 45° is lower than + 25°, which justifies the higher lateral resistance of the latter. The negative battered minipiles also carry axial load, yet their lateral resistance is lower than vertical minipiles due to partial mobilisation of skin friction at the same lateral displacement. While *p*-multipliers are one approach to estimating piles' lateral load capacity, as demonstrated earlier, it requires further verification for shallow-depth

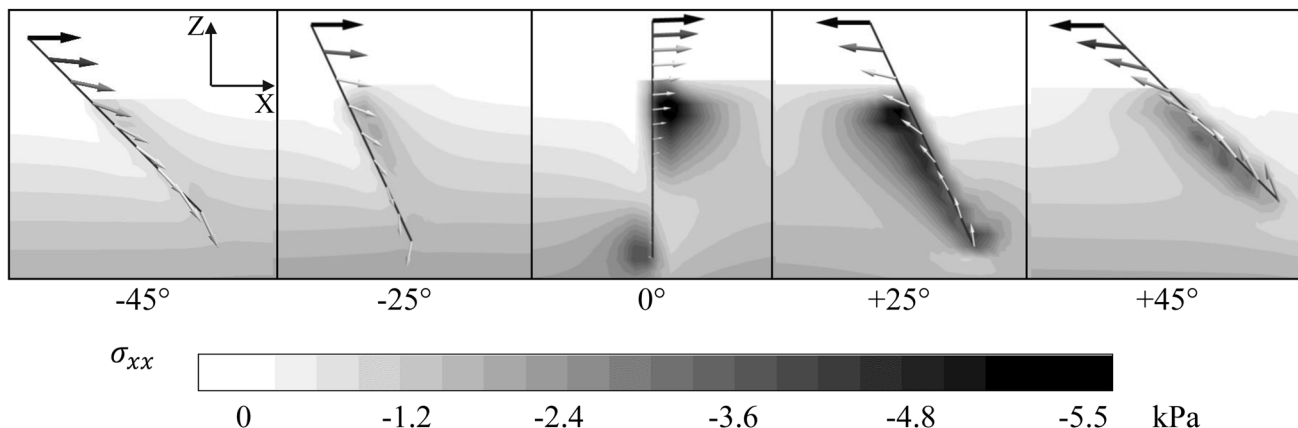


Fig. 15 Stress contour and minipile node displacement profile at 2 mm lateral head displacement

minipiles. Hence, an analytical method is proposed in this study, which is presented next.

4 Analytical solution

The experimental analysis presented earlier demonstrates the soil–structure interaction and the force–displacement behaviour of the minipiles. While proposing a p -multiplier (Ω) is one of the common techniques to predict the lateral behaviour of battered piles, it requires further investigation for shallow-depth battered minipiles, as seen from the numerical simulation. Therefore, to further incorporate the current findings into practice, a classical analytical solution is adopted and developed further to predict the ultimate lateral load.

The relative stiffness of the vertical minipile at 90% relative density is first identified using Eq. 1. For a hollow minipile with I_p of $3.12 \times 10^{-10} \text{ m}^4$ and E_p of $2 \times 10^{11} \text{ N/m}^2$, the relative stiffness factor (K_{rs}) is 0.00395, so the model minipiles can be characterised as semi-rigid (or at proximity to the maximum threshold for flexible piles). Meyerhof et al. [44] stated that a flexible pile behaves as a rigid pile up to a critical depth D_{eu} , which can be determined using Eq. 7.

$$D_{eu} = f_u K_{rs}^{0.12} L \text{ provided } \frac{D_{eu}}{D} \leq 1, \quad (7)$$

where K_{rs} is the relative stiffness factor, L is the embedded depth of the pile and $f_u = 1.65$ and 1.5 for sand and clay, respectively [44]. For the K_{rs} of 0.00395, and embedded pile depth of 0.27 m, D_{eu} is calculated to be 0.23 m from the soil surface.

4.1 Lateral load on vertical minipile

The ultimate lateral load capacity of a vertical pile can be estimated from the area of passive soil pressure distribution as proposed by Meyerhof and Sastry [43] for flexible piles,

$$Q_h = (0.12\gamma D_{eu} K_{br} + 0.4c K_{cr}) B D_{eu} \quad (8)$$

where Q_h is the ultimate transversal load, B is the diameter of the pile, c is the cohesion or undrained shear strength, γ is the unit weight of the soil, and K_{br} and K_{cr} are the net lateral soil pressure coefficients and can be obtained from Meyerhof [41]. For rigid piles, Prasad and Chari [51] proposed,

$$Q_h = 0.24 \left[10^{(1.3 \tan \varphi + 0.3)} \right] \gamma x B \{0.27x - 1.7L\} \quad (9)$$

where x is the point of the rotation of the rigid pile and can be determined using the relation in Prasad and Chari [51].

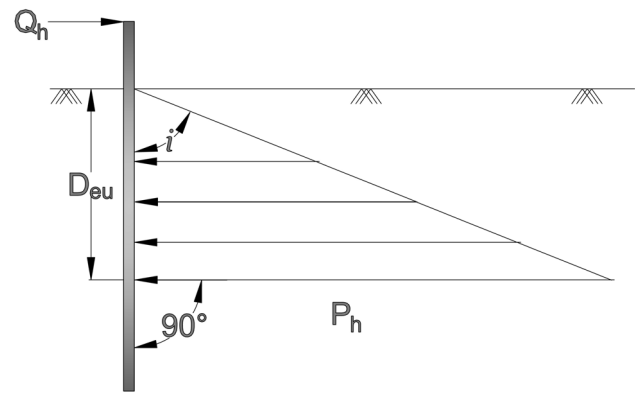


Fig. 16 Soil pressure distribution for vertically installed minipile

The passive soil wedge's shape depends on the piles' relative stiffness and can be measured with instrumentation such as pressure transducers. For cohesionless soil, where c is zero, the passive soil pressure distribution along the pile is assumed to be triangular [37, 41, 51], with zero at the top increasing linearly to P_h at the base, at a depth of D_{eu} [43] (Fig. 16). Their shape can also be determined from the bending moment profile using p - y curves as explained in the previous section.

4.2 Lateral load on battered minipile

4.2.1 Load decomposition

The load acting on the battered minipiles can be decomposed into axial and lateral components. The subjected lateral load, Q_{hi} , can be decomposed into two components, as depicted in Fig. 17. As shown in Fig. 17, Q_h is the lateral load acting perpendicularly to the minipile shaft and resisted by lateral soil pressure (P_h), and the other resisting component is Q_v , the axial load acting along the pile shaft resisted by the skin friction (P_v).

Q_v is estimated from the skin friction along the pile shaft using the method proposed by Hanna and Nguyen [26] for cohesionless soil and battered piles as follows,

$$Q_v = p_p K_{s(ave)} \tan \delta_{m(ave)}^L \gamma' z dz \quad (10)$$

where p_p is the perimeter of the pile, $K_{s(ave)}$ is the mobilised coefficient of earth pressure equivalent to $R \cdot K_{ave}$ where R is the reduction factor, K_{ave} is the average coefficient of earth pressure, $\delta_{m(ave)}$ is the average mobilised angle of interface friction, γ' is the effective unit weight of soil and z is the depth of soil. The value of K_{ave} corresponding to the batter angle and R corresponding to the ratio of interface friction angle to internal friction angle can be deduced from the figures proposed by Caquot and Kerisel [16], as shown in Hanna and Nguyen [26].

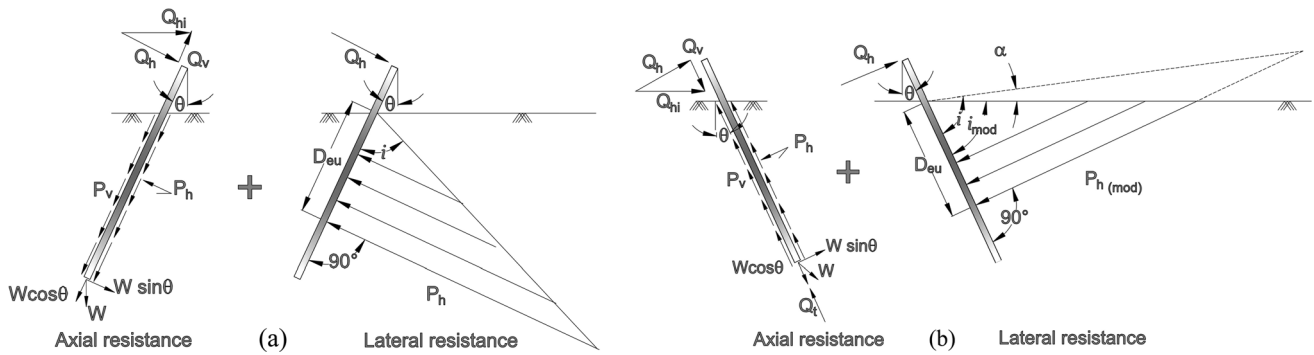


Fig. 17 Soil pressure distribution for a positive and b negatively battered minipile

4.2.2 Positive battered minipile

For a pile with positive batter, based on the load decomposition, the axial load acts away from the pile and hence, is counteracted by the skin friction acting downwards along the pile shaft (Fig. 17a). The passive pressure acting in front of the pile is also inclined away from the ground surface. Thus, the equation for ultimate lateral load capacity Q_{hi} of a battered pile is,

$$Q_{hi} = (Q_h + W \sin \theta) \cos \theta + (Q_v - W \cos \theta) \sin \theta \quad (11)$$

where Q_h is the ultimate lateral load of the vertically installed minipile and W is the self-weight of the minipile. The cosine and sine components of the self-weight get balanced with each other and, hence, are omitted from Eq. 11.

4.2.3 Negative battered minipile

As stated earlier, in the case of a positively battered minipile, the pressure wedge is inclined away from the soil surface, which allows the entire wedge to be formed. For negative battered minipiles, Fig. 17b depicts that the skin friction acts upward along the pile shaft. In the case of soil plugging, the toe capacity (Q_t) also contributes to Q_{hi} along with the skin friction; however, for minipiles, it is neglected, considering their small diameter. The passive pressure wedge is inclined towards the ground surface. The triangle’s base is not completely mobilised as the triangular pressure distribution hypothetically occurs above the soil surface. This reduction in pressure distribution can be thus quantified using a passive pressure angle of ‘ i ’ where, for the vertical case, ‘ i ’ can be defined from Fig. 16.

From the pressure distribution for the vertical case,

$$\tan(i) = \frac{P_h}{D_{eu}} \quad (12)$$

where P_h is the maximum pressure acting at the depth, D_{eu} .

The net area of the soil pressure distribution with P_h at the base gives the ultimate lateral resistance of vertical minipile, Q_h . Hence, $\tan(i)$ can also be written as,

$$\tan i = \frac{2 * Q_h}{D_{eu}^2} \quad (13)$$

where Q_h is the ultimate lateral load capacity of the vertically installed minipile.

The soil boundary limits the pressure wedge when the pressure distribution is inclined towards the ground surface. Thus, the angle ‘ i ’ needs to be modified to consider the altered wedge shape bound by the ground surface and hence can be termed as ‘ i_{mod} .’ α is then defined as the angle by which the pressure wedge rotates above the ground surface; therefore, $i_{mod} = i - \alpha$, and ‘ θ ’ is the degree of batter. Thus, using trigonometry,

$$\alpha = i_{mod} + \theta - 90^\circ \quad (14)$$

$$\text{so, } i_{mod} = i - \alpha = 90^\circ - \theta \quad (15)$$

$$\text{and } P_{h(mod)} = \tan(i_{mod}) \times D_{eu} \quad (16)$$

where $\theta > (90^\circ - i)$,

Hence, the ratio of modified to actual soil pressure at the base is,

$$\frac{P_{h(mod)}}{P} = \frac{\tan(90 - \theta)}{\tan(i)} \quad (17)$$

so, a new reduction factor (RF) is introduced to quantify this modification and can be defined as,

$$RF = \frac{\tan(90 - \theta)}{\tan(i)} \quad (18)$$

This RF accounts for the reduced passive pressure for negative battered minipiles.

Hence, the modified term to determine the lateral resistance due to soil pressure on negatively battered minipiles would be $Q_h \cos \theta \times RF$, and the ultimate lateral load will be given by,

$$Q_{hi} = Q_h \cos \theta \times RF + Q_v \sin \theta \quad (19)$$

Table 4 Value of components involved in predicting ultimate lateral load at 90% D_r

Angle	Q_v (N)	$Q_v \sin\theta$ (N)	Positive battered		Negative battered		
			$Q_h \cos\theta$ (N)	Q_{hi} (N)	RF	$Q_h \cos\theta$ (N)	Q_{hi} (N)
0°	38.9	0.0	20.0	20.0	1.000	20.0	20.0
15°	28.9	7.5	19.3	26.8	0.005	0.10	7.6
25°	30.0	12.7	18.1	31.6	0.003	0.05	12.7
30°	31.8	15.9	17.3	33.2	0.002	0.04	16.0
45°	19.3	13.7	14.1	27.8	0.001	0.02	13.7

This proposed analytical method was used to predict the lateral load-carrying capacity of the experimentally tested minipiles in dense sand (90% D_r) for various batter angles. In this study, the analytically predicted load for vertical, positive and negative battered minipile coincided with the displacement criteria of 20% of B , as stated earlier based on Brom’s criteria (1964). The values of the components for respective batter angles, according to Eq. 19, are delineated in Table 4. The experimentally observed capacities were 34 N, 25.2 N, 12 N and 10 N, respectively, for + 25°, + 45°, – 25° and – 45° minipiles. The predicted ultimate lateral loads are 31.6 N, 27.8 N, 12.7 N and 13.7 N for + 25°, + 45°, – 25° and – 45°, which are in good agreement with the observed values.

The frictional component has a pronounced effect on the ultimate lateral load capacity of battered minipiles. In the case of battered minipiles, the optimum capacity occurs for the minipiles battered at $\pm 30^\circ$, which can be attributed to the higher skin friction ($Q_v \sin \theta$ in Table 4). If the skin friction is factored down for all the cases (e.g., when the pile shaft is smooth or the relative density of the sand is lower), the increment in the load capacity for the positive batter is not very prominent. Thus, it can be deduced that the effect of pile batter in loose sand is not as significant, which was also found experimentally (Fig. 9b) and previously stated by Zhang et al. [65].

4.3 Verification of the analytical method with full-scale test results in clay

This section validates the proposed analytical model’s ability to predict the ultimate lateral load for battered minipiles in clayey soil. The field test results were adopted from Mondal et al. [46], where full-scale minipiles with a diameter of 42.4 mm and a length of 1.6 m were tested in a clayey site under lateral loading. The site was characterised by cone penetration tests that consisted of medium stiff clay with no water table up to 6 m of depth. Since the depth of penetration of the minipiles was only 1.3 m with a

vertical eccentricity of 0.30 m above the soil surface, the soil properties were averaged for simplification. The average cohesion, unit weight and Young’s modulus up to the penetration depth were 38 kPa, 19 kN/m³ and 14 MPa, respectively, using the methods described in Mondal et al. [46]. The minipiles were installed using a handheld jackhammer at batter angles of 0°, + 25° and – 25° with the vertical. The force and displacement at the minipile head were measured using a load cell and linear displacement transducers, respectively (more detail about field testing can be found in Mondal et al. [46]). The lateral load for + 25°, 0° and – 25° at 0.2*B* displacement (8 mm for full-scale minipiles) is 7 kN, 4.2 and 3.2 kN, respectively.

The E_{SL} of the soil (based on Vesic’s 1961 formula as explained in Mondal et al. [47]) and the K_{rs} were calculated to be 6.3 MPa and 1.4×10^{-4} , respectively, categorising the minipile as flexible. The effective embedment depth, D_{eu} , calculated using Eq. 7, was 0.67 m. The analytical method was utilised to estimate the ultimate load for full-scale minipiles similar to the physical model minipiles. The experimentally obtained Q_h for vertically installed minipiles was 4.2 kN. Adopting the soil properties as mentioned earlier, the unit skin friction was evaluated for cohesive soil using Focht and Vijayvergiya [22],

$$f_{av} = \lambda(\bar{\sigma}'_o + 2c_u) \tag{20}$$

where λ is the coefficient that varies with the penetration depth of the pile, $\bar{\sigma}'_o$ is the average effective vertical stress for the entire pile embedment length and c_u is the mean undrained shear strength. The total skin friction is thus,

$$Q_v = f_{av} \times \pi BL \cos\theta \tag{21}$$

The estimated skin friction for various batter angles and the predicted ultimate lateral load for the full-scale minipiles are summarised in Table 5. The predicted lateral load capacity of + 25° and – 25° are 7 and 3.3 kN, respectively, and those obtained experimentally are 7 and 3.2 kN, respectively. The very good agreement between the

Table 5 Predicted ultimate lateral load using the analytical solution for full-scale battered minipiles

Angle	Q_v (kN)	$Q_v \sin\theta$ (kN)	Positive battered		Negative battered		
			$Q_h \cos\theta$ (kN)	Q_{hi} (kN)	RF	$Q_h \cos\theta$ (kN)	Q_{hi} (kN)
0°	6.9	0.0	4.2	4.6	1.00	4.20	4.2
15°	6.8	1.8	4.1	6.0	0.20	0.84	2.6
25°	6.7	2.8	3.8	7.0	0.11	0.48	3.3
30°	6.6	3.3	3.6	7.5	0.09	0.39	3.7
45°	6.2	4.4	3.0	8.6	0.05	0.22	4.6

experimental and the predicted ultimate load proves the analytical method's suitability for semi-rigid and flexible minipiles in cohesionless and cohesive soil.

4.4 Impact of batter angle

As explained earlier, a new reduction factor was proposed, and the lateral load-carrying capacities (Q_{hi}) of experimentally tested minipiles battered at positive and negative battered minipiles in sand and clay were predicted (summarised in Table 4 and Table 5). When the lateral load and skin friction are compared with increasing batter angle, the lateral load component ($Q_h \cos \theta$) decreases as the batter angle increases. However, the skin friction ($Q_v \sin \theta$) is maximum at 30° for sand and 45° for clay. This combination gives an optimum angle of $\pm 30^\circ$ and $\pm 45^\circ$ for sand and clay, respectively, only for the adopted minipile properties, and this optimum batter angle is expected to vary with the pile properties. For a particular soil type (either cohesionless or cohesive), the optimum batter angle depends on the shear strength of the soil as well as the properties of the pile, such as diameter, length and relative stiffness (as shown for clay [47]). It should be noted that the optimum batter angle observed here is for a range of batter angles between $\pm 0^\circ$ to $\pm 45^\circ$ only.

The plot in Fig. 18a compares the ratio of the ultimate load at respective batter angles to the ultimate lateral capacity of the vertical model minipile in this study with results from the literature in cohesionless soil. In Fig. 18a, the ultimate load reaches a maximum at an optimum angle of 30° for the positive batter case, as also reported by Kyung and Lee [32]. However, for the negative case, Kyung and Lee [32] indicated a monotonous decreasing pattern, while Sharma et al. [59] presented an increment

with batter angle, which is again highly dependent on the slenderness ratio of the pile and is well captured by the analysis proposed in this study. The predicted full-scale ultimate lateral load ratio is compared with the limited data on battered piles in clay [55, 56] and plotted in Fig. 18b. The comparison of the predicted lateral capacity of the battered minipiles in this study with the limited experiments in clay results shows similar trend.

Although the soil and pile properties studied here differ, the load predicted by the analytical solution depicts a pattern similar to that reported in the literature. Hence, the ability of the analytical method to predict the ultimate lateral load for two pile geometries in clayey and sandy soil establishes its reliability.

The calibrated numerical model was further simulated to perform a parametric study of the model and prototype minipiles in both cohesive [47] and cohesionless soil. The ultimate loads observed from the numerically produced force–displacement curves of the respective cases were in very good agreement with those predicted using the analytical method (results not shown here for brevity). Thus, while computing the ultimate lateral load capacity, the mobilised passive pressure and skin friction play an indispensable role. This analytical method uses the ultimate lateral capacity of vertically installed minipiles (which can be obtained experimentally or using classical analytical methods). It accurately predicts the ultimate lateral load of shallow-depth battered minipiles. The proposed method considers soil properties, including relative density for sandy soil and cohesive strength for clayey soil, and hinges on the relative stiffness of the minipile.

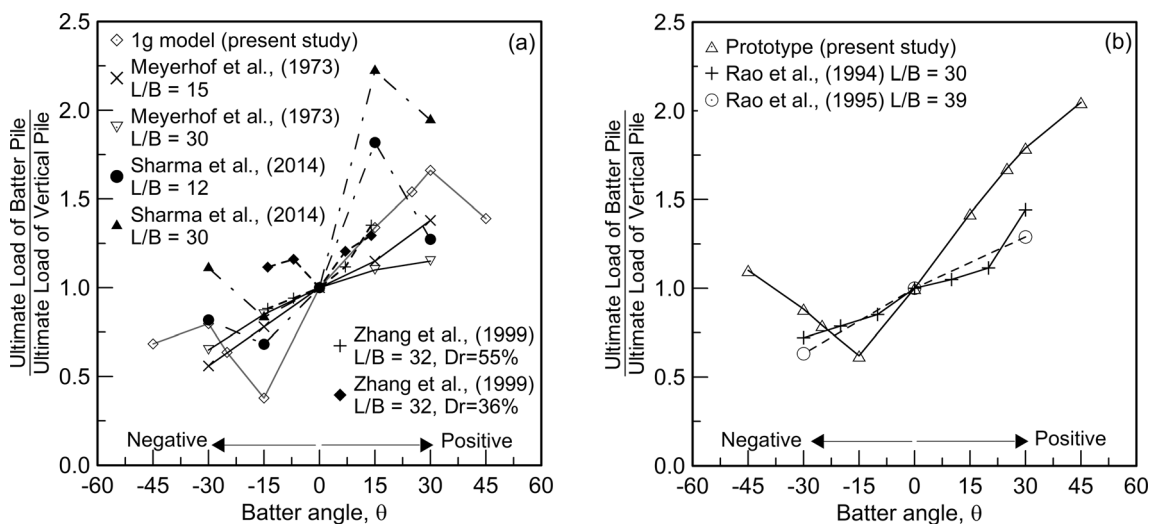


Fig. 18 Comparison of predicted ultimate lateral load ratio for various battered angles in **a** sand and **b** clay

5 Conclusion

The lateral load-bearing mechanism of driven minipiles installed at 0° , $+25^\circ$, $+45^\circ$, -25° and -45° was investigated in this study using a 1g physical model at 90% and 75% relative density of sand. An optic fibre-based instrumentation technique was adopted to obtain the strain profile along the model minipile shaft at different loading stages. The maximum load-carrying capacity in dense sand was observed for $+25^\circ$ followed by $+45^\circ$ and 0° , respectively, and -25° and -45° showed lower capacity than the vertically installed minipile. A similar trend was also noted for 75% relative density, except that there was a lower divergence in lateral resistance for various batter angles.

From the calibrated numerical model, bending moment, axial force, stress contours and p - y curves were obtained. The $+25^\circ$ semi-rigid minipile carried the maximum lateral load and sustained lesser bending than 0° and, hence, could be recommended to have optimum performance capability. The p - y curves plotted at $5B$ depth from the soil surface showed higher passive pressure for 0° ; however, the passive pressure for $+25^\circ$ was higher than 0° at a pile depth of $10B$ from the soil surface. It can be noticed that with the increase in lateral head deflection, the ratio of ultimate soil reaction for all battered angles also increases.

The analytical solution proposed in this study accurately predicts the ultimate lateral resistance of shallow-depth battered minipiles, and the presented method accounts for both pile and soil properties. The shape of the passive pressure wedge is the first of the two key discriminating factors between the lateral load capacity of the positive and negative group of battered minipiles. The second contributing factor to higher transversal resistance of battered piles/minipiles is axial resistance or skin friction, which was quantified here. The skin friction component was highest at 30° for sand and 45° for clay, influencing the optimum batter angle under lateral load in different soil conditions. The analytical method's reliability and robustness were verified with experimental results in both cohesive and cohesionless soil for flexible and semi-rigid minipiles, respectively, and hence can be implemented in practice.

Acknowledgements This research was funded by the Australian Research Council Linkage scheme (project ID LP160100828). In addition, the authors acknowledge the financial and in-kind support provided by Surefoot Pandoe Pty Ltd. The first author thanks The University of Melbourne for offering the Melbourne Research Scholarship.

Author contributions All authors contributed to the study conception and design. Material preparation, data collection and analysis were performed by SM. The first draft of the manuscript was written by SM and MD commented on previous versions of the manuscript.

Reviewing, editing and supervision were done by MD. All authors read and approved the final manuscript.

Funding Open Access funding enabled and organized by CAUL and its Member Institutions. This research was funded by the Australian Research Council Linkage scheme (project ID LP160100828). In addition, the authors acknowledge the financial and in-kind support provided by Surefoot Pandoe Pty Ltd.

Data availability All of the data and models that support the findings of this study are available from the corresponding author upon request.

Code availability The numerical (FLAC) codes are available from the corresponding author upon request.

Declarations

Conflict of interest The authors have no conflicts of interest to declare that are relevant to the content of this article.

Ethical approval Not applicable.

Consent for publication Not applicable.

Open Access This article is licensed under a Creative Commons Attribution 4.0 International License, which permits use, sharing, adaptation, distribution and reproduction in any medium or format, as long as you give appropriate credit to the original author(s) and the source, provide a link to the Creative Commons licence, and indicate if changes were made. The images or other third party material in this article are included in the article's Creative Commons licence, unless indicated otherwise in a credit line to the material. If material is not included in the article's Creative Commons licence and your intended use is not permitted by statutory regulation or exceeds the permitted use, you will need to obtain permission directly from the copyright holder. To view a copy of this licence, visit <http://creativecommons.org/licenses/by/4.0/>.

References

1. FLAC 3D Manual: a computer program for fast Lagrangian analysis of continua. Minneapolis, Minnesota, USA.
2. Abadie CN, Byrne BW, Houlby GT (2019) Rigid pile response to cyclic lateral loading: laboratory tests. *Géotechnique* 69(10):863–876
3. Abd Elaziz AY, El Naggar MH (2015) Performance of hollow bar micropiles under monotonic and cyclic lateral loads. *J Geotech Geoenviron Eng* 141(5):04015010
4. Airey DW, Wood D (1987) An evaluation of direct simple shear tests on clay. *Géotechnique* 37(1):25–35
5. Al Tarhouni MA, Hawlader B (2021) Monotonic and cyclic behaviour of sand in direct simple shear test conditions considering low stresses. *Soil Dyn Earthq Eng* 150:106931
6. Altaee A, Fellenius BH (1994) Physical modeling in sand. *Can Geotech J* 31(3):420–431. <https://doi.org/10.1139/t94-049>
7. Armour, T., Groneck, P., Keeley, J., Sharma, S., (2000) Micropile design and construction guidelines: Implementation manual, United States. Federal Highway Administration
8. Ashour M, Alaaeldin A, Arab MG (2020) Laterally loaded battered piles in sandy soils. *J Geotech Geoenviron Eng* 146(1):06019017

9. Ashour M, Norris G, Pilling P (1998) Lateral loading of a pile in layered soil using the strain wedge model. *J Geotech Geoenviron Eng* 124(4):303–315. [https://doi.org/10.1061/\(asce\)1090-0241\(1998\)124:4\(303\)](https://doi.org/10.1061/(asce)1090-0241(1998)124:4(303))
10. ASTM D4253–16e1, (2019) Standard Test Methods for Maximum Index Density and Unit Weight of Soils Using a Vibratory Table. ASTM International, West Conshohocken, PA
11. ASTM D4254–00, (2017) Standard Test Methods for Minimum Index Density and Unit Weight of Soils and Calculation of Relative Density. ASTM International, West Conshohocken, PA
12. Awoshika K (1971) Analysis of foundation with widely spaced batter piles. University of Texas, Austin
13. Baek SH, Kim J, Lee SH, Chung CK (2018) Development of the cyclic p–y curve for a single pile in sandy soil. *Marine Georesour Geotech* 36(3):351–359
14. Bjerrum L, Landva A (1966) Direct simple-shear tests on a Norwegian quick clay. *Geotechnique* 16(1):1–20
15. Broms BB (1964) Lateral resistance of piles in cohesionless soils. *J Soil Mech Foundations Div* 90(3):123–158
16. Caquot, A., Kerisel, L., (1948) *Traite de mecanique des sols*. Gauthier Villars, Paris, Gauthier Villars. Paris
17. Chakraborty T, Salgado R (2010) Dilatancy and shear strength of sand at low confining pressures. *J Geotech Geoenviron Eng* 136(3):527–532
18. Coyle HM, Castello RR (1981) New design correlations for piles in sand. *J Geotech Eng Div* 107(7):965–986
19. Doherty P, Igoe D, Murphy G, Gavin K, Preston J, Mcavoy C, Byrne BW, Mcadam R, Burd HJ, Houlby GT, Martin CM, Zdravković L, Taborda DMG, Potts DM, Jardine RJ, Sideri M, Schroeder FC, Muir Wood A, Kallehave D, Skov Gretlund J (2015) Field validation of fibre Bragg grating sensors for measuring strain on driven steel piles. *Geotech Lett* 5(2):74–79. <https://doi.org/10.1680/geolett.14.00120>
20. Dong J, Chen F, Zhou M, Zhou X (2018) Numerical analysis of the boundary effect in model tests for single pile under lateral load. *Bull Eng Geol Env* 77:1057–1068
21. Fleming K, Weltman A, Randolph M, Elson K (2008) *Piling engineering*. CRC Press, Boca Raton, FL
22. Focht, J. A., Vijayvergiya, V., (1972) A new way to predict capacity of piles in clay, *Offshore Technology Conference, Offshore Technology Conference*
23. Fukui, J., (2006) Performance of seismic retrofits with high capacity micropiles, *Proceedings of the 7th International Workshop on Micropiles, Lizzi Lecture*, pp. 1–14.
24. Goit CS, Saitoh M, Igarashi T, Sasaki S (2021) Inclined single piles under vertical loadings in cohesionless soil. *Acta Geotech* 16(4):1231–1245. <https://doi.org/10.1007/s11440-020-01074-9>
25. Guo Z, Khidri M, Deng L (2019) Field loading tests of screw micropiles under axial cyclic and monotonic loads. *Acta Geotech* 14(6):1843–1856. <https://doi.org/10.1007/s11440-018-0750-6>
26. Hanna A, Nguyen TQ (2003) Shaft resistance of single vertical and batter piles driven in sand. *J Geotech Geoenviron Eng* 129(7):601–607. [https://doi.org/10.1061/\(ASCE\)1090-0241\(2003\)129:7\(601\)](https://doi.org/10.1061/(ASCE)1090-0241(2003)129:7(601))
27. Hong Y, He B, Wang L, Wang Z, Ng CWW, Mašin D (2017) Cyclic lateral response and failure mechanisms of semi-rigid pile in soft clay: centrifuge tests and numerical modelling. *Can Geotech J* 54(6):806–824
28. Hong C-Y, Zhang Y-F, Zhang M-X, Leung LMG, Liu L-Q (2016) Application of FBG sensors for geotechnical health monitoring, a review of sensor design, implementation methods and packaging techniques. *Sensors Actuators A: Phys* 244:184–197. <https://doi.org/10.1016/j.sna.2016.04.033>
29. Kubo, K., (1965) Experimental study of the behavior of laterally loaded piles., *Proceedings of the VI International Conference on Soil Mechanics and Foundation Engineering*, Montreal, Canada, pp. 275–279.
30. Kyung D, Kim D, Kim G, Lee J (2017) Vertical load-carrying behavior and design models for micropiles considering foundation configuration conditions. *Can Geotech J* 54(2):234–247
31. Kyung D, Lee J (2017) Uplift load-carrying capacity of single and group micropiles installed with inclined conditions. *J Geotech Geoenviron Eng* 143(8):04017031
32. Kyung D, Lee J (2018) Interpretative analysis of lateral load-carrying behavior and design model for inclined single and group micropiles. *J Geotech Geoenviron Eng* 144(1):04017105
33. Leblanc C, Houlby G, Byrne B (2010) Response of stiff piles in sand to long-term cyclic lateral loading. *Géotechnique* 60(2):79–90
34. Lee J, Kyung D, Hong J, Kim D (2011) Experimental investigation of laterally loaded piles in sand under multilayered conditions. *Soils Found* 51(5):915–927. <https://doi.org/10.3208/sandf.51.915>
35. Lee W, Lee W-J, Lee S-B, Salgado R (2004) Measurement of pile load transfer using the fiber Bragg grating sensor system. *Can Geotech J* 41(6):1222–1232. <https://doi.org/10.1139/t04-059>
36. Li G-W, Pei H-F, Yin J-H, Lu X-C, Teng J (2014) Monitoring and analysis of PHC pipe piles under hydraulic jacking using FBG sensing technology. *Measurement* 49:358–367. <https://doi.org/10.1016/j.measurement.2013.11.046>
37. Lin H, Ni L, Suleiman MT, Raich A (2015) Interaction between laterally loaded pile and surrounding soil. *J Geotech Geoenviron Eng* 141(4):04014119
38. Lizzi F (1978) Reticulated root piles to correct landslides. *American Society of Civil Engineers, Chicago, ASCE Convention*, pp 23–31
39. Matlock H, Reese LC (1962) Generalised solutions for laterally loaded piles. *Trans Am Soc Civ Eng* 127(1):1220–1247
40. Mesri G, Hayat T (1993) The coefficient of earth pressure at rest. *Can Geotech J* 30(4):647–666
41. Meyerhof G (1995) Behaviour of pile foundations under special loading conditions: 1994 RM Hardy keynote address. *Can Geotech J* 32(2):204–222
42. Meyerhof GG, Ranjan G (1973) The bearing capacity of rigid piles under inclined loads in sand II: Batter piles. *Canadian Geotech J* 10(1):71–85
43. Meyerhof G, Sastry V (1985) Bearing capacity of rigid piles under eccentric and inclined loads. *Canadian Geotech J* 22(3):267–276. <https://doi.org/10.1139/t85-040>
44. Meyerhof G, Sastry V, Yalcin A (1988) Lateral resistance and deflection of flexible piles. *Canadian Geotech J* 25(3):511–522. <https://doi.org/10.1139/t88-056>
45. Meyerhof G, Yalcin A (1984) Pile capacity for eccentric inclined load in clay. *Can Geotech J* 21(3):389–396
46. Mondal S, Disfani M, Mehdizadeh A (2023) Behaviour of bio-inspired grouped battered minipiles under lateral loading in clay. *Acta Geotech (In press)*. <https://doi.org/10.1007/s11440-023-02019-8>
47. Mondal S, Disfani M, Narsilio GA (2022) Battered minipiles in fine-grained soils: Soil-structure interaction. *Comput Geotech* 147:104762. <https://doi.org/10.1016/j.compgeo.2022.104762>
48. Othonos A (1999) Fiber bragg gratings. *Fund Appl Telecommun Sensing*. <https://doi.org/10.1063/1.1148392>
49. Poulos HG (1982) Single pile response to cyclic lateral load. *J Geotech Eng Div* 108(3):355–375
50. Poulos HG, Davis EH (1980) *Pile foundation analysis and design*. Wiley, New York
51. Prasad YV, Chari T (1999) Lateral capacity of model rigid piles in cohesionless soils. *Soils Found* 39(2):21–29
52. Rad NS, Tumay MT (1987) Factors affecting sand specimen preparation by raining. *Geotech Test J* 10(1):31–37

53. Randolph, M. (1980) PIGLET: A computer programme for the analysis and design of pile groups under general loading conditions. Soil Report TR91, CUED/D, Cambridge Univ.
54. Rao SN, Ramakrishna V, Rao MB (1998) Influence of rigidity on laterally loaded pile groups in marine clay. *J Geotech Geoenviron Eng* 124(6):542–549
55. Rao, S. N., Veeresh, C., (1994) Influence of pile inclination on the lateral capacity of batter piles in clays, The Fourth International Offshore and Polar Engineering Conference, International Society of Offshore and Polar Engineers
56. Rao, S. N., Veeresh, C., (1995) Behaviour of Instrumented Model Batter Piles In Clays, The Fifth International Offshore and Polar Engineering Conference, International Society of Offshore and Polar Engineers
57. Sastry V, Meyerhof G (1990) Behaviour of flexible piles under inclined loads. *Can Geotech J* 27(1):19–28. <https://doi.org/10.1139/t90-003>
58. Sharma B, Hussain Z (2019) Behaviour of batter micropiles subjected to vertical and lateral loading conditions. *J Geosci Environ Protect* 7(02):206. <https://doi.org/10.1080/19386362.2018.1564181>
59. Sharma, B., Zaheer, S., Hussain, Z., (2014) Experimental model for studying the performance of vertical and batter micropiles, Geo-Congress 2014 American Society of Civil Engineers
60. Simpson B, Hoult NA, Moore ID (2015) Distributed sensing of circumferential strain using fiber optics during full-scale buried pipe experiments. *J Pipeline Syst Eng Practice* 6(4):04015002. [https://doi.org/10.1061/\(ASCE\)PS.1949-1204.0000197](https://doi.org/10.1061/(ASCE)PS.1949-1204.0000197)
61. Tak Kim B, Kim N-K, Jin Lee W, Su Kim Y (2004) Experimental load–transfer curves of laterally loaded piles in Nak-Dong River sand. *J Geotech Geoenviron Eng* 130(4):416–425. [https://doi.org/10.1061/\(asce\)1090-0241\(2004\)130:4\(416\)](https://doi.org/10.1061/(asce)1090-0241(2004)130:4(416))
62. Wang Y, Mok C (2008) Mechanisms of small-strain shear-modulus anisotropy in soils. *J Geotech Geoenviron Eng* 134(10):1516–1530
63. Wang X, Ye A, Shafieezadeh A, Li J (2018) Shallow-layer py relationships for micropiles embedded in saturated medium dense sand using quasi-static test. *Geotech Test J* 41(1):193–206
64. Xu D, Huang F, Rui R (2020) Investigation of single pipe pile behavior under combined vertical and lateral loadings in standard and coral sands. *Int J Geosynth Ground Eng* 6(2):1–10
65. Zhang L, Mcvay MC, Lai PW (1999) Centrifuge modelling of laterally loaded single battered piles in sands. *Can Geotech J* 36(6):1074–1084. <https://doi.org/10.1139/t99-072>

Publisher's Note Springer Nature remains neutral with regard to jurisdictional claims in published maps and institutional affiliations.